

Direct Observation of Heterogeneous Formation of Amyloid Spherulites in Real-time by Super-resolution Microscopy

Nikos Hatzakis (✉ hatzakis@nano.ku.dk)

University of Copenhagen

Min Zhang

University of Copenhagen, Denmark <https://orcid.org/0000-0002-2797-5049>

Henrik Pinholt

University of Copenhagen

Xin Zhou

University of Copenhagen

Søren Bohr

University of Copenhagen,

Luca Banetta

Polytechnic University of Turin

Alessio Zaccone

University of Milan

Vito Foderà

University of Copenhagen

Article

Keywords: Super-resolution imaging, protein aggregation, spherulites, real-time, REPLOM.

Posted Date: February 15th, 2022

DOI: <https://doi.org/10.21203/rs.3.rs-1338225/v1>

License:   This work is licensed under a Creative Commons Attribution 4.0 International License.

[Read Full License](#)

Version of Record: A version of this preprint was published at Communications Biology on August 20th, 2022. See the published version at <https://doi.org/10.1038/s42003-022-03810-1>.

1 Direct Observation of Heterogeneous Formation of
2 Amyloid Spherulites in Real-time by Super-
3 resolution Microscopy

4 *Min Zhang¹, Henrik D. Pinholt¹, Xin Zhou², Søren S.-R. Bohr¹, Luca Banetta³, Alessio Zaccone⁴,*
5 *Vito Foderà^{2,*} and Nikos S. Hatzakis^{1,5,*}.*

6 ¹Department of Chemistry, Faculty of Science, University of Copenhagen, Denmark

7 ²Department of Pharmacy, Faculty of Health and Medical Sciences, University of Copenhagen,
8 Denmark

9 ³Department of Applied Science and Technology, Polytechnic University of Turin, Italy

10 ⁴Department of Physics, University of Milan, Italy

11 ⁵ NovoNordisk centre for Protein research, Faculty of Health and Medical Sciences University of
12 Copenhagen, Denmark

13 **KEYWORDS:** Super-resolution imaging, protein aggregation, spherulites, real-time, REPLOM.

14

15

16 **Abstract**

17 The misfolding of proteins and their aggregation in the form of fibrils or amyloid-like spherulites
18 are involved in a spectrum of pathological abnormalities. Our current understanding of protein
19 amyloid aggregation mechanisms has primarily relied on the use of spectrometric methods to
20 determine the average growth rates and diffraction limited microscopes with low temporal
21 resolution to observe the large-scale morphologies of intermediates. We developed a REal-time
22 kinetics via binding and Photobleaching LOcalisation Microscopy (**REPLOM**) super-resolution
23 method to directly observe and quantify the existence and abundance of diverse aggregate
24 morphologies of the model system insulin, below the diffraction limit and extract their
25 heterogeneous growth kinetics. Our results revealed that even the growth of a microscopically
26 identical aggregates, e.g. amyloid spherulites, may follow distinct pathways. Specifically,
27 spherulites do not exclusively grow isotropically but, surprisingly, may also grow anisotropically,
28 following similar pathways as reported for minerals and polymers. Combining our technique with
29 machine learning approaches, we associated growth rates to specific morphological transitions and
30 provided energy barriers and the energy landscape at the level of single aggregate morphology.
31 Our unifying framework for the detection and analysis of spherulite growth can be extended to
32 other self-assembled systems characterized by a high degree of heterogeneity, disentangling the
33 broad spectrum of diverse morphologies at the single-molecule level.

34

35

36 **Introduction**

37 Protein misfolding is a hallmark of a number of devastating conditions, such as Alzheimer's and
38 Parkinson's disease¹⁻³. Moreover, insulin aggregates have been found deposited at diabetic
39 patients' insulin injection sites⁴. As one of the important aggregates, amyloid spherulites have
40 been found in the brain tissues in connection with the onset and progression of Alzheimer's
41 disease^{2,3}. In addition, they may also present opportunities to develop advanced materials for drug
42 delivery⁵. Spherulites ranging from a few micrometers to several millimeters in diameter can form
43 both *in vivo* and *in vitro* and are observed during the aggregation of multiple proteins including
44 insulin, that we used as a model system here^{3,6,7}. These aggregates are characterized by a
45 fascinating core-shell morphology and seem to be the result of a general self-assembly process that
46 is common to metal alloys⁸, minerals⁹, and polymers^{10,11}. While we have a solid understanding
47 of the fibrillar growth kinetics¹², the mechanisms of the formation and growth of spherulites is
48 still limited¹³⁻¹⁵.

49 The studies of protein spherulite formation primarily rely on spectrometric evidence for their
50 average growth rates^{13,16}. Considering that a high heterogeneity of aggregate populations may
51 present within the same self-assembly reaction¹⁷, bulk methods provide limited information on
52 the aggregation kinetics of individual species, in the form of either fibrils or spherulites, averaging
53 the effect of the morphological heterogeneity of the aggregate population. Fluorescent microscopy,
54 as an intuitive and non-invasive method, has been used more and more in the area of protein
55 aggregation to record the growth intermediates¹⁵ and to observe the final structures¹⁸. While the
56 direct observation of fibril growth and time lapses of spherulite growth with temporal resolution
57 of minutes was recently reported for A β peptides^{15,19-21}, the kinetic analysis of individual
58 aggregates mainly focuses on fibrils, which challenges the evaluation of the kinetics of the multiple
59 and concurrent pathways. Meanwhile, due to the complex structures of spherulites, the resolution
60 of diffraction-limited microscopy such as TIRFM or confocal microscopy is not sufficient to
61 decipher the details of spherulites^{15,22,23}. Super-resolution methods surpass the diffraction
62 limitations, albeit often provide snapshots of the growth or the final morphology of fibrils²⁴⁻²⁶
63 offering limited information on the temporal development of diverse structures.

64 Here we developed a method named Real-time kinetics via binding and Photobleaching
65 Localisation Microscopy (**REPLOM**) to directly observe the formation of individual protein
66 amyloid structures using human insulin (HI) as a model system. Attaining real-time videos of the
67 spherulite growth process allowed to reconstruct the super-resolution images of the spherulites and
68 their growth kinetics. Using homemade software based on Euclidian minimum spanning tree and
69 machine learning clustering ²⁷⁻³¹, we quantitatively associated the growth rates to specific
70 morphological transitions during growth, eventually extracting detailed energy barriers and, thus,
71 the energy landscape for each type of aggregation morphology. Our data on astigmatism-based 3D
72 direct stochastic optical reconstruction microscopy (dSTORM) ³², spinning disk confocal
73 microscopy ³³, and scanning electron microscopy (SEM) confirm that the presence of
74 heterogeneous structures is not artefact of our method. Our combined results allowed us to
75 differentiate among the different species in solution and decipher the nature, morphology and
76 abundance of individual spherulites at different growth stages. Surprisingly, we found that HI
77 spherulite growth is not exclusively isotropic and may occur anisotropically. We anticipate that
78 the framework presented here will serve as a unique and generic methodology for the simultaneous
79 detection and analysis of multiple species within a single self-assembly reaction. In the specific
80 case of protein systems, the aggregation of which is related to degenerative diseases, our approach
81 provides a platform for connecting kinetics, morphological transitions, and structure and further
82 aid our understanding on interventions against degenerative diseases.

83 **Results and Discussion**

84 **Direct observation of diverse structures of HI spherulites by 3D dSTORM, SEM and** 85 **spinning disk microscopy**

86 We thermally induced insulin amyloid aggregation using an established protocol ³⁴ and examined
87 the bulk kinetics by detecting the fluorescence of the amyloid-sensitive dye Thioflavin T (ThT)
88 and the turbidity signal (Figure S1a). The kinetics traces at incubation temperature of 60 °C, show
89 the classical three-step profile, with the reaction reaching completion after only 3-4 hours. The
90 turbidity and ThT signal perfectly overlapped, suggesting that the aggregation reaction was
91 entirely of an amyloid-like origin ³⁵. Cross-polarized microscopy recordings of the characteristic
92 Maltese cross, indicating spherulite formation under these conditions ⁷ (Figure S2). However,

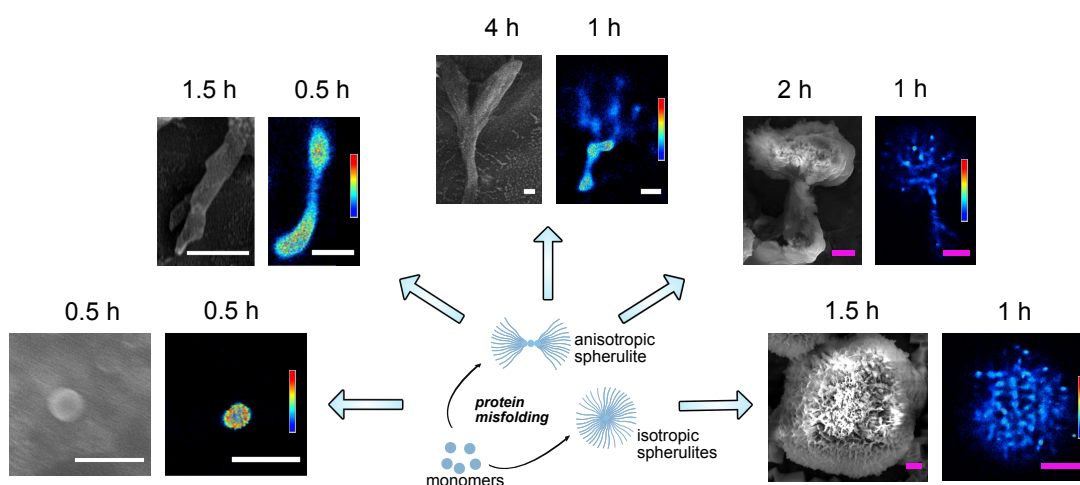
93 standard analysis of the bulk ThT signal was unable to provide information on the morphological
94 transition occurring during the reaction.

95 To observe directly and with high-resolution the diverse structures of insulin aggregates, we
96 combined the insights obtained from SEM and 3D dSTORM. Using 3D dSTORM allowed us to
97 extend beyond diffraction-limited imaging by TIRF microscopy, which may mask spherulite shape
98 and growth directionality³² (Figure 1). Recordings at incubation times between 0.5 to 4 hours
99 points (see methods) provided direct recordings of the diverse early species that can co-exist at the
100 same incubation time. We found spherical-like protein condensates of approximately 200 nm in
101 diameter formed after 0.5 hours, while, a linear pattern was observed with incubation times ranging
102 between 0.5-1h. Surprisingly, the recordings beyond the diffraction limit revealed that at longer
103 incubation times the commonly observed spherulites were found to co-exist in the mixture with
104 anisotropically grown structures (Figure 1, Figure S4, S5c and S5d).

105 The fact that both SEM and 3D dSTORM methods identified the same particle morphology
106 supports this not to be an artifact of fluorescence microscopy, fluorophore labeling (Figure S1b),
107 sample drying for SEM imaging (Figure 1). Note however that depending on conditions the
108 distribution of morphologies may vary slightly consistent with earlier reporting of electrostatic
109 effect for A β -(1-40)¹⁵ (see Figure S5f). Extending beyond the diffraction limit suggest that protein
110 spherulite growth may diverge from isotropically grown in space^{7,36}, and proceed in a preferential
111 direction.

112 The density plots created with 3D dSTORM (Figure 1) clearly showed that the core had a much
113 higher density than the branching parts, consistent with previous suggestions of the existence of a
114 low-density corona in spherulite structures^{7,37}. The formation of the high-density cores appears to
115 indicate the nucleation point, with the subsequent linear-like elongation and branching of slender
116 threadlike fibrils resembling crystalline growth^{38,39}. This is consistent with the recently proposed
117 initial protein condensation process⁴⁰, and further growth is determined by tight fibril packing,
118 which forces the biomolecular assembly to occur anisotropically along one specific direction.
119 Delineating this however would require additional experiment and is beyond the scope of this
120 study. The directly observed anisotropy challenges the isotropic spherulite growth, for which the
121 process occurs via the formation of a radiating array of fiber crystallites, but it is observed in the

122 case of crystalline-coil block copolymer spherulites⁴¹. The origin of such anisotropy might be due
 123 to the occurrence of secondary and heterogeneous nucleation at the aggregate surface^{20,42}, with
 124 different binding efficiencies depending on the aggregate areas. While the data in Figure 1 would
 125 be consistent with the secondary nucleation, deciphering this with additional data falls beyond the
 126 scope of this work.

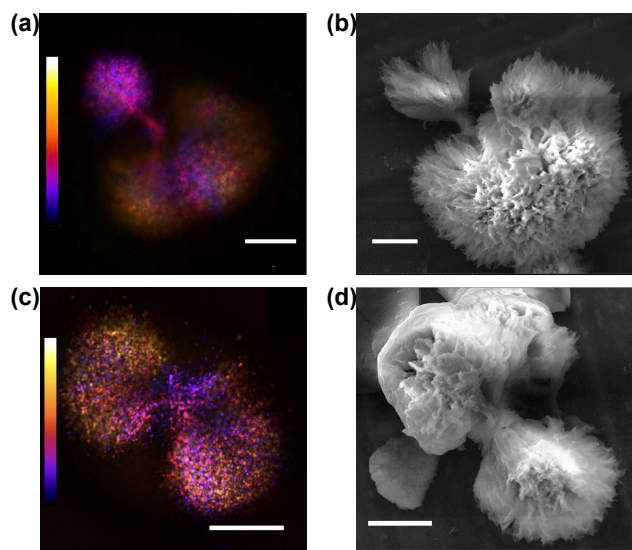


127
 128 **Figure 1. SEM and super-resolution 3D dSTORM reconstructed images of the co-existing in solution**
 129 **morphologies of the anisotropically/isotropically grown structures of different HI aggregates.** 3D dSTORM
 130 images: density plots, pseudocolor scale corresponds to neighbor localisations: the density of neighboring events
 131 within a 100-nm radius sphere from localization. Pseudocolor scale ranges from 0 to 1000 for the first image on left
 132 and 0 to 400 for the rest. Scale bars in white color are 1 μm and scale bars in purple color are 5 μm .

133
 134 The diameter of the early linear aggregates increased as a function of time (Table S1). This
 135 indicates that the growth was not limited to end-to-end attachment to the linear aggregate, and
 136 lateral aggregation also took place. While this is to a certain extent expected²⁰, the super resolution
 137 recordings allowed its quantification. The early central linear structures, with diameters of $400 \pm$
 138 100 nm (see Table S1), successively branched to form radially oriented amyloid fiber-like
 139 structures. The further away from the core, the higher the increase in branching frequency, yielding
 140 more space-filling patterns. The dimensions of the corona-like structure were $\sim 2 \mu\text{m}$ to $>20 \mu\text{m}$,
 141 as shown in Figure 1.

142 To exclude that diverse morphologies originate from electrostatic interactions with surface
 143 immobilization^{15,43}, we used spinning disk microscopy and SEM to detect the morphology of

144 spherulites at different growth stages in solution (see Figure S5). Consistent with the data displayed
145 in Figure 1, we detect both spherulites with asymmetrically grown (Figure 2a and 2b) and
146 symmetrically grown (Figure 2c and 2d) lobes supporting (see 3D videos of Figure 2a and 2c in
147 Supplementary Movies. S1 and S2). We confirmed that the asymmetric growth was not an artifact
148 of substrate depletion, as spherulites with asymmetric lobes had already formed by 2 hours of
149 incubation (Figure 1). This suggests that growth periods of multiple rates occurred within a single
150 sample (Figure S5), which may be masked in bulk kinetics. Moreover, our data indicated the
151 possibility that growth did not occur entirely isotropically from the central core, but rather, there
152 was initially a preferential direction.



153
154 **Figure 2. Structure of anisotropically grown human insulin spherulites of two distinct growth-morphologies.** a)
155 and b) Spherulites with two asymmetric sides captured by spinning disk confocal microscopy and SEM, respectively.
156 c) and d) Spherulites with symmetric two side structures captured by spinning disk confocal microscopy and SEM,
157 respectively. Data in (a) and (c) were acquired for a sample from incubation time of 16 h at 60 °C. Data in (b) and (d)
158 are for a sample from an incubation time of 4 h at 60 °C. Color scales are from $-14.04\ \mu\text{m}$ to $14.04\ \mu\text{m}$ in (a) and
159 $-8.46\ \mu\text{m}$ to $8.46\ \mu\text{m}$ in (c). Scale bars are $10\ \mu\text{m}$. All samples were covalently labeled with Alexa Fluor 647.

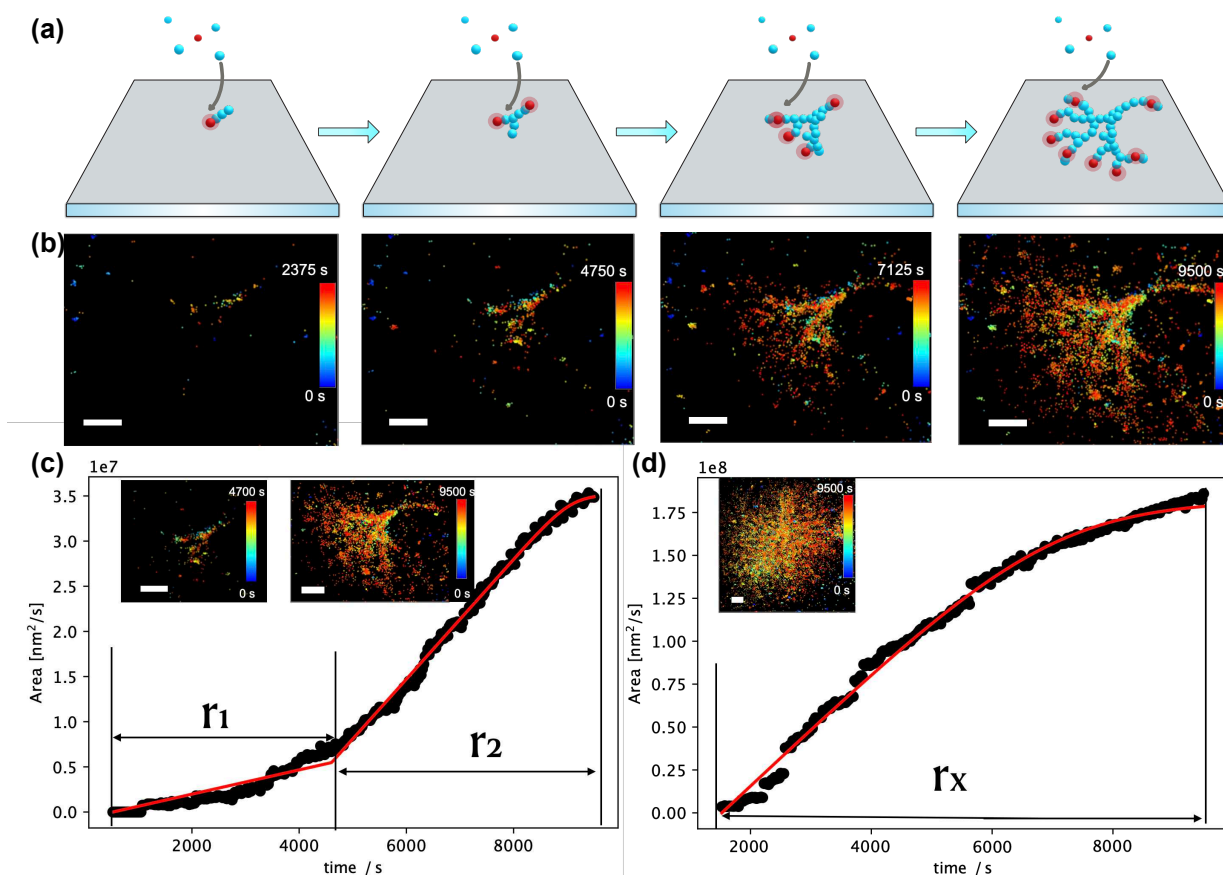
160
161 **REPLOM: a super resolution method for the real time direct observation of growth of**
162 **protein aggregation**

163 We developed a new super-resolution experimental method based on single-molecule
164 localisation microscopy, to quantitatively measure the growth rates at the single-aggregate level

165 while simultaneously monitoring the morphological development of the structure. We named the
166 method REal-time kinetics via binding and Photobleaching LOcalisation Microscopy (REPLM),
167 as it allows researchers, for the first time, to directly image the morphological development of each
168 individual aggregates in real-time with super-resolution and, simultaneously, access the kinetic
169 traces for thermodynamic analysis of the process. To perform REPLM, HI monomers were
170 covalently labeled with Alexa Fluor 647 NHS Ester (see Supplementary Information for
171 experimental details). Figure 3a illustrates how REPLM works: initially, only small protein
172 condensates, i.e., cores, are formed and bind to the poly-L-lysine-covered surface. The spatial
173 location of each of the fluorophores is accurately detected prior to their photobleaching ^{44,45}.
174 Optimizing the imaging settings and the absence of imaging buffer ensures rapid chromophore
175 bleaching after binding (see Methods and Figure S8). As the growth progresses, additional HI
176 monomers from the solution bind to the core, extending the dimensions of the aggregate. Each
177 labeled insulin binding event results in a diffraction-limited spot, the precise location of which can
178 be accurately extracted, similarly to in photoactivated localization microscopy (PALM)
179 methodologies ⁴⁶ (see Methods and Figure S9 for resolution of the method and Supplementary
180 Movie S3-S4).

181 Parallelized recordings of the spatially distinct binding of multiple individual HI loaded with
182 emitters allow the real-time direct observation of the temporal morphological development of each
183 aggregate (see Figure 3b, Figure S10, and Supplementary Movies, S3-S4). Due to the slow kinetics
184 of spherulite formation, the waiting time between each frame was 20-40 seconds, which allowed
185 to capture both seed formation and extract the growth rate of insulin aggregates. Faster frame rates
186 such as 20 ms are possible for the fast grown aggregates. The methodology is reliant on the intrinsic
187 bleaching of chromophores to extract their coordinates ⁴⁷⁻⁴⁹ and is similar to Binding Activation
188 Localisation Microscopy (BALM) ⁵⁰, which measures existing structures, but additionally
189 facilitates real-time direct observation of the growth process. It also extends beyond recent
190 methods based on conventional TIRF to observe exclusively fibril growth ²⁰ or low temporal
191 resolution time lapses of linear or spherulite growth ^{15,19,21}, offering in addition rate recording and
192 morphological development of both fibrillar and spherulite structures even below the diffraction
193 limit. Consequently, the geometry and morphological development of each aggregate can be

194 observed directly with sub-diffraction resolution, offering the extraction of each particle's growth
195 kinetics.



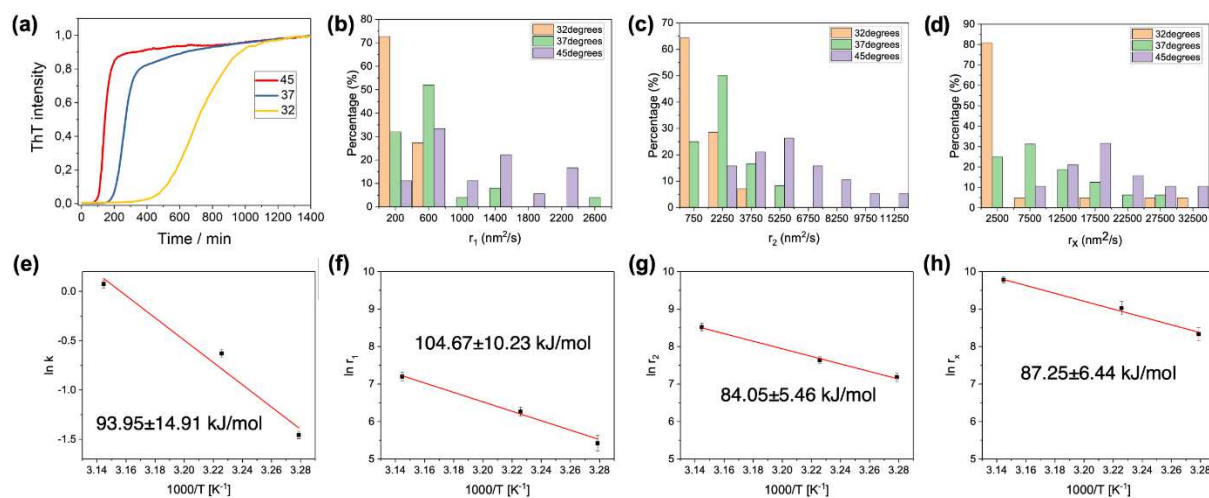
196

197 **Figure 3. Direct real-time observation of HI aggregate growth by REPLOM (real-time kinetics via binding**
198 **and photobleaching localisation microscopy).** a) Cartoon representation of REPLOM: initially, the fluorescent
199 signal from the small fluorescently labeled protein condensates was detected, followed by chromophore
200 photobleaching. As the growth progressed, labeled insulins from solution bound to the aggregate, increasing the
201 dimensions. Each binding event resulted in a diffraction-limited spot, the coordinates of which were accurately
202 extracted, before it was photobleached by the intense laser. Parallelized recordings of the spatially distinct binding
203 of multiple individual emitters revealed the temporal morphological development of several aggregates (Red is
204 Alexa Fluor 647-labeled HI in fluorescent state, and blue is un-labeled insulin or Alexa Fluor 647-labeled HI in
205 dark/photobleached state). b) Direct real-time observation of temporal development of anisotropic growth at $t =$
206 2375 time intervals. Scale bars: 2 μm . c) and d) Growth curves of anisotropic spherulite (c) and isotropic spherulite
207 (d). For anisotropic spherulites, the curve contains two parts roughly correlating with the formation of the core/linear
208 part and branching part (see method REPLOM section). Isotropic spherulite growth was linear and followed by
209 saturation. Inset: the corresponding HI spherulite obtained by REPLOM. Scale bars: 2 μm . See SI for the movies.

210

211 **Extraction of growth rates for diverse aggregate morphologies**

212 Consistent with the 3D dSTORM data, the direct observation of HI spherulite growth by
 213 REPLOM confirmed that HI spherulites grow both anisotropically and isotropically (Figure 3). To
 214 extract the growth rate kinetics for each individual aggregate, we identified the points belonging
 215 to the growing aggregate with an approximate Euclidean Minimum Spanning tree segmentation⁵¹
 216 and estimated the area using a Gaussian mixture model based on hierarchical clustering in Figure
 217 3c and 3d (see Supporting Information for the details)²⁷⁻³⁰. For isotropic morphologies, a single
 218 linear growth rate was observed (r_x) followed by a plateau (see Supporting Information), while for
 219 anisotropic morphologies the growth curve consisted of two rate components (r_1 and r_2), as shown
 220 in Figure 3c and 3d and Figure S11; r_1 corresponds to the initial linear core and r_2 to the branching
 221 part, and they best fitted to reaction-limited linear growth and a diffusion-limited sigmoidal
 222 growth, respectively^{14,16,52-54} (see Methods and Supplementary Movies S3-S8). Consequently, the
 223 growth rates (r_1 , r_2 , and r_x) for each individual aggregate were extracted. The growth readouts of
 224 the individual geometrically distinct morphologies allowed us to go beyond the standard analysis
 225 of sigmoidal curves, which does not yield information on, or discriminate between, the temporal
 226 developments for each morphology. REPLOM revealed that the anisotropic growth operated via a
 227 two-step process imposed by the geometry of the growth—a pattern masked in current super-
 228 resolution and bulk readouts.



229

230 **Figure 4. Kinetic and thermodynamic characterization of insulin aggregation** a) Normalized bulk ThT
 231 fluorescence kinetics on with incubation temperatures of 45, 37, and 32 °C. b) and c) REPLOM-extracted rate
 232 distribution of anisotropic aggregates at the three different incubation temperatures: (b) linear part and (c) branching
 233 part. d) Rate distribution of isotropic aggregates at the three different incubation temperatures. e-h) Arrhenius plots

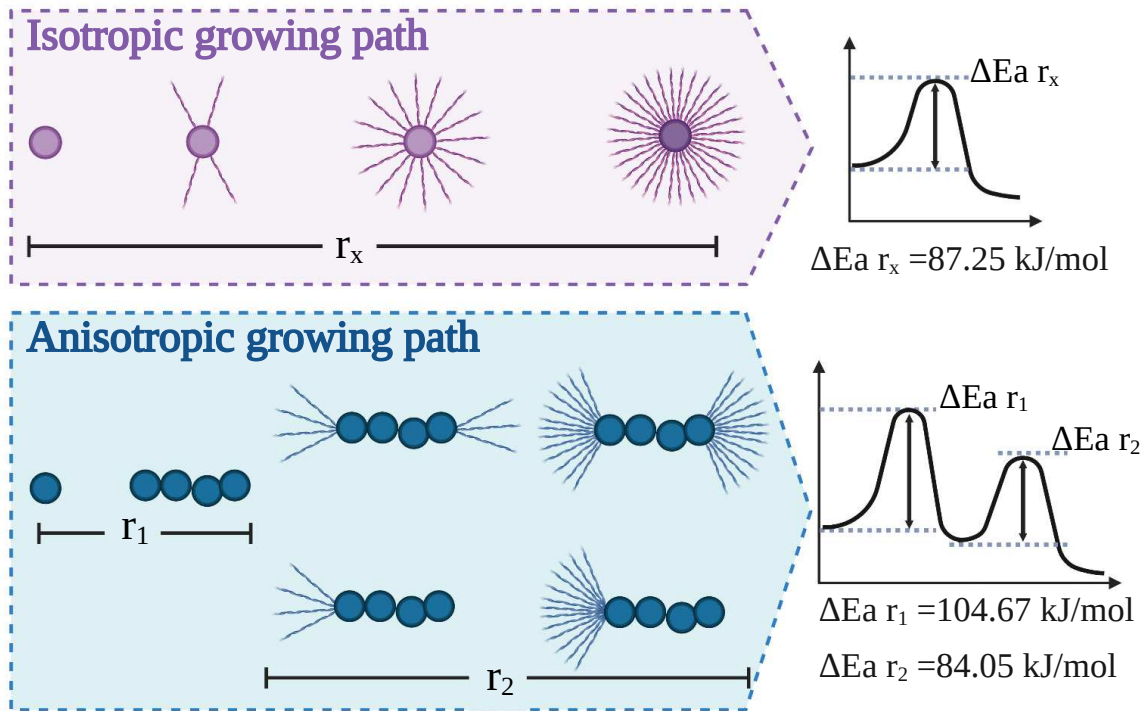
234 for spherulites obtained from bulk experiments (e), and REPLOM (f-h). The formation of linear (f) and branched (g)
235 parts of anisotropic spherulites, and the formation of isotropic spherulites (h).

236

237 **Extraction of Energy barriers for the growth of diverse HI spherulites morphologies**

238 The real-time single-particle readout from REPLOM facilitates the kinetic analysis of the
239 temperature dependence of growth for each diffraction limited type of spherulite morphology and,
240 consequently, the extraction of the activation energy barriers for both the spherulite morphologies
241 and growth phase. Therefore, HI aggregate formation was induced at three different temperatures
242 accessible without introducing optical artefacts in our microscopy setup: 45 °C, 37 °C, and 32 °C.
243 The ThT fluorescence measurements at the three temperatures representing the average growth
244 kinetics are shown in Figure 4a. The rate distributions at the three temperatures for each type of
245 morphological growth are shown in Figure 4 b, 4c, and 4d ($N = \sim 20$, see also Figure S12). As
246 expected, the linear parts r_1 (Figure 4b) and branched parts r_2 (Figure 4c), as well as the isotropic
247 growth rate r_x (Figure 4d), increased at increased incubation temperature. The data do not show a
248 pronounced curvature, and this may be due to the narrow temperature range investigated in our
249 study and is in agreement with earlier studies⁵⁵. This would suggest that the differences in heat
250 capacity between the soluble states of the proteins and the transition states for aggregation are
251 small ⁵⁵. Using the Arrhenius equation ^{55,56} (Figure 4e-4h), we extracted the activation energy of
252 each of the isotropic or anisotropic morphological growths and the respective linear or branching
253 part of the individual aggregates. For the linear part of the anisotropic spherulites, the activation
254 energy was 104.67 ± 10.23 kJ/mol (Figure 4f), while for the branched part it was 84.05 ± 5.46
255 kJ/mol (Figure 4g), and for the isotropically grown spherulites it was 87.25 ± 6.44 kJ/mol (Figure
256 4h). The activation energy extracted from the bulk kinetics shown in Figure 4e (93.95 ± 14.91
257 kJ/mol) is consistent with data on bovine insulin fibril formation (~ 100 kJ/mol) ⁵⁵. The REPLOM
258 methodology on the other hand allowed deconvolution of a higher barrier related to step 1 in the
259 anisotropic growth (r_1) and lower barrier in the branching part of isotropic and anisotropic growth
260 (r_x and r_2). Together, these data indicate that the pronounced heterogeneity of growth mechanisms
261 and structures within the aggregation ensemble leads to heterogeneity of the activation barriers.
262 We indeed highlighted that spherulite growth may proceed both isotropically and anisotropically,
263 with the latter presenting a two-step process imposed by the geometry of the growth and

264 characterized by two activation energies that are markedly different to those obtained by bulk
 265 kinetics and for insulin fibrils⁵⁵.



266

267 **Figure 5. Schematic representation of the diverse pathways of insulin aggregation and their respective energy**
 268 **barriers** Top: Isotropic spherulite growth, where fibril-like filaments isotropically and radially grow on a dense core.
 269 Process is characterized by a single activation energy of $\sim 87 \text{ kJ/mol}$. Bottom: anisotropic growth, where the dense core
 270 is growing linearly before it successively branches to form radially oriented amyloid fiber-like structures. The
 271 further the branching from the core, the more increased the branching frequency, yielding a more space-filling pattern.
 272 The process involves two steps imposed by the geometry of the growth and characterized by two activation energies
 273 of 104 and 84 kJ/mol for the linear and branching parts, respectively.

274

275 Conclusions

276 Our combined results revealed that the growth of amyloid core-shell structures for insulin, i.e.,
 277 spherulites, may proceed not only via isotropic growth but also by following a multistep pathway
 278 characterized by initial pronounced anisotropic behavior (Figure 5). The anisotropic growth may
 279 thus not be an exclusive property of metal alloys, salts and minerals, but may extend to protein
 280 aggregates. In essence are data are consistent with a unifying mechanism underlying chemical
 281 growth of both biological soft materials and hard-non biological composites. Such variability in
 282 growth within the same aggregation reaction results in a spectrum of aggregation kinetics traces

283 that can be quantitatively detected by our method, allowing the operator to extract the
284 thermodynamic parameters for each of the aggregation subsets. These findings underscore how
285 conclusions solely based on bulk kinetics data may overlook the complexity and heterogeneity of
286 the aggregation process.

287 Our novel experimental approach offers real-time detection of super-resolution images during
288 protein aggregation kinetics. The REPLOM method allows the direct observation of self-assembly
289 kinetics at the level of single aggregates and the quantification of the heterogeneity of aggregates
290 and their growth mechanisms, which are otherwise masked with current methodologies. Our
291 general framework can be extended to the simultaneous detection of markedly different structures
292 within a single aggregation reaction and contribute to research into a more comprehensive
293 representation of the generalized energy landscape of proteins. This will offer the unique
294 possibility of disentangling different mechanisms leading to the myriad of aggregate structures
295 that occur. The method is implemented on the insulin model systems, but can be easily translatable
296 to more medically relevant proteins, such as α -synuclein or A β peptide. Deciphering whether these
297 structures persist in the context of the cellular environment and the direct physiological
298 implications of anisotropically grown morphologies would require combination of our
299 methodologies with DNA-paint and antibodies as recently developed⁵⁷. Our approach may indeed
300 provide unprecedented information on transient intermediate species, which are nowadays
301 recognized as the cause of progression in many diseases, in terms of both energetics and
302 morphology. Finally, our approach is general and may be applicable to generic self-assembly
303 reactions of systems characterized by a high degree of heterogeneity.

304 **Methods-Microscopy**

305 **Spinning Disk Microscopy.**

306 The 3D images of grown spherulites were taken by a SpinSR10-spinning disk confocal super
307 resolution microscope (Olympus) using a silicone oil-immersion 100x objective
308 (UPLSAPO100XS, NA=1.35, Olympus). The Alexa Fluor 647-labeled HI spherulites were excited
309 with a 640 nm laser (OBIS COHERENT). The exposure time was 50 ms and the z step length was
310 0.36 μm .

311 **Scanning Electron Microscopy (SEM).**

312 SEM images of spherulites were taken by using a Quanta FEG 200 ESEM microscope.

313 **Cross Polarized Microscopy.**

314 Images were collected using a 10x objective and crossed polarised which enabled spherulites to
315 show the characteristic Maltese cross (Zeiss Axioplan Optical Microscope, Carl Zeiss).

316 **Super-resolution Imaging**

317 Super resolution imaging was attained on an inverted Total Internal Reflection microscope (TIRF)
318 (Olympus IX-83) with a 100x oil immersion objective (UAPON 100XOTIRF, NA=1.49,
319 Olympus) Alexa Fluor 647 was excited by a 640 nm solid state laser line (Olympus) and reflected
320 to a quad band filter cube (dichroic mirrors ZT640rdc, ZT488rdc and ZT532rdc for splitting and
321 with single-band bandpass filters FF02-482/18-25, FF01-532/3-25 and FF01-640/14-25). Signal
322 was detected by an EMCCD camera (imagEM X2, Hamamatsu).

323 **3D direct Stochastic Optical Reconstruction Microscopy (3D dSTORM) and image**
324 **analysis.**

325 3D dSTORM imaging was achieved by installing a cylindrical lens ($f = 500$ mm) in the emission
326 pathway of (TIRF) to introduce the astigmatism of point spread function (PSF)³². All the
327 dSTORM imaging experiments were performed at room temperature (21 °C). The exposure time
328 was 30 ms and 10000 frames for each movie.

329 To extract z information from the widths of single molecule images, we generated a calibration
330 curve of PSF width in the lateral plane (W_x and W_y) as a function of height by measuring Atto
331 655-labeled liposomes using TIRF with a step size of 10 nm and exposure time of 30 ms (Fig. S3).

332 The HI aggregates which were incubated in a block heater for 0.5 hours to 2 hours at 60 °C. At the
333 desired time they were added to the poly-L-Lysine treated microscope chamber⁵⁸ and incubated
334 for 10 min at room temperature to ensure immobilization. Extra sample was washed away with
335 MilliQ water. Imaging buffer containing 50 mM Tris, 10 mM NaCl, 10% (w/v) glucose, 0.5
336 mg/mL glucose oxidase, 40 µg/mL catalase and 0.1 M MEA⁵⁹ was flushed into the chamber for
337 dSTORM imaging. All measurements were carried out at room temperature. The optimal ratio of
338 labeled to unlabeled insulin that provided reliable signal without affecting the aggregation process
339 or compromising resolution was 1 to 60,000. This is quite different from earlier dSTORM imaging

340 of fibrils using a ratio of 1/20²⁴ because of the much higher 3D density of spherulites that prevent
341 reliable super resolution imaging at high labeling ratios.

342 The 3D dSTORM data was analysed by ThunderSTORM⁶⁰. The z information of individual
343 localisations was extracted based on the calibration curves (calculated by ThunderSTORM, shown
344 in Figure S3). The detected localisations were further filtered according to their intensity and drift
345 correction, in order to remove some possible false positive or poor quality detections. 3D super-
346 resolution images were visualized with ViSP software⁶¹.

347 **REal-time kinetic via Photobleaching Localisation Microscopy (REPLOM)**

348 **Preparation of HL aggregates and imaging.** The solution containing 5 mg/mL HI monomer
349 was first incubated in a block heater to skip the lag phase. The optimal pre-incubation time for
350 spherulite formation on the microscope surface was found to be ~ 8 hours for 45 °C, 20 hours for
351 37 °C and 75 hours for 32 °C, respectively. Then they were transferred to poly-L-lysine coated
352 glass slide chambers and covered by a lip to prevent solvent evaporation during imaging (Figure
353 S6).

354 REPLOM was performed on the same TIRF microscope setup as the 3D STORM without the
355 cylindrical lens. Alexa Fluor 647 labeled HI was excited by 640nm solid state laser lines
356 (Olympus). We found the optimal ratio of labeled to unlabeled insulin for REPLOM to be ca. 1 to
357 10,000. A high labelling density would result in proximate fluorophores from the newly grown
358 area emitting simultaneously and therefore cause mislocalization²⁴. Too low labeling ratio may
359 cause some details, e.g. small branching part, during spherulites growth to be undetected. Imaging
360 was performed with an exposure time of 30 ms followed by a waiting time for each frame of 20-
361 40 seconds so as to capture in real time the slow kinetics of spherulite formation. This frame rate
362 allowed to capture both seed formation and extract the growth rate of insulin aggregates. Faster
363 frame rates may be required for different protein aggregates⁶². All image acquisition was
364 performed at the same incubation temperatures as in the block heater. The incubation temperatures
365 during the imaging processes were achieved by a heating unit 2000 (PECON).

366 **Data analysis.** The data was analysed by ThunderSTORM. Some possible false positive or poor-
367 quality detections were removed by intensity filter. Figure S7 shows the comparison of images

368 prior to and after drift correction. The reconstructed images with time series were obtained by
369 ViSP⁶¹ software. For Quantification of growth kinetics is available in Supporting Information.

370 **Lifetime of fluorophores.** The lifetime of fluorophores in REPLOM was evaluated by checking
371 the duration time of fluorescent state before they were photobleached. We checked 1885 individual
372 Alexa Fluor 647 fluorophores and found they were photobleached very fast without imaging buffer
373 (Figure S7). The lifetime is about 0.7845 ± 0.0017 frames.

374 **Resolution of REPLOM.** The resolution of REPLOM was determined by the FWHM of single
375 spot's intensity (Figure S9) using an adapted version of previously published software^{45,63}. Briefly,
376 using our subpixel resolution software, we were able to extract multiple (91) single spots (see
377 Figure S9) and align all to the same center. Fitting a two-dimensional gaussian to the resulting
378 stacked clusters allowed the reliable extraction of FWHM used to determine the obtained
379 resolution. Using a maximum likelihood fitting scheme avoided potential bias from data binning.

380 **Quantification of growth kinetics by Euclidean Minimum Spanning tree.** The method for
381 identification of candidates for fluorophores docking on a growing aggregate was inspired by
382 recent published work⁵¹ and done in the following way:
383 First, using all detected RE-PLOM spots from the movie, an approximate Euclidean Minimum
384 Spanning tree was constructed using only the 30 nearest neighbors as candidates for edges.
385 Regions of aggregate candidates were cut from each other by removing all edges with lengths more
386 than the 95th percentile. This is an effective way of separating high-density regions from low-
387 density regions. The computation was done using the function HierarchicalClustering from the
388 astroML python package. Since we were interested mostly in the large insulin aggregates where
389 the internal structure was visible, it was decided that all clusters obtained in this manner with less
390 than 100 detected fluorophores were excluded from the subsequent analysis.

391 The time-dependency of the aggregate growth was found by a similar approach. At each frame,
392 for a cluster, a refined grouping was done by cutting an approximate Euclidean Minimum
393 Spanning tree made using 10 neighbors with a distance cutoff of 400nm which was found to be
394 optimal for removal of most spots outside the aggregate while still not cutting up the main group.
395 The points from the largest subgroup resulting from this analysis were defined to be the aggregate
396 for that frame.

397 The area of the aggregate was estimated using a gaussian mixture model with a component for
398 every 5 points in the aggregate, but not less than 25 components ⁵¹ . We defined the area of the
399 aggregate as the region lying above the average probability density in this fit. The growth profile
400 resulting from our approach had a few artifacts like jumps and fluctuations due to mixture model
401 fitting and aggregate segmentation, but we found that the resulting growth curve in most cases had
402 an identifiable trend, and the results were quite consistent across parameter choices.

403 From the estimated area of the aggregate in each frame, a growth curve could be plotted.

404 The radial growth rate of such aggregates has previously been found to be either reaction-limited
405 or diffusion-limited, leading to linear increase in time or increase as $\propto \sqrt{t}$ respectively ^{14,52-54} . If
406 we assume that the estimated area of the aggregated is directly related to the radius as $A \propto R^2$ the
407 two growth types lead to the following models

408

409
$$\frac{dA(t)}{dt} = r_1 ,$$

410

411
$$\frac{dA(t)}{dt} = \frac{1}{2} r_1 t .$$

412

413 Where the first model is diffusion limited and the second is reaction limited. We found that many
414 of the structures were initially consistent with reaction limited diffusion and then shifted to either
415 diffusion or reaction limited growth with a new rate. To allow for this shift, we let the growth be
416 diffusion limited up to a switch-point t_0 after which the growth rate changes. We formulate one
417 such model which ends reaction limited and one which remains diffusion limited

418

419
$$\frac{dA(t)}{dt} = \begin{cases} r_1, & t_0 > t \\ r_2, & t_0 \leq t \end{cases} ,$$

420
$$\frac{dA(t)}{dt} = \begin{cases} r_1, & t_0 > t \\ \frac{1}{2} r_2 t, & t_0 \leq t \end{cases} .$$

421

422 Finally, without continuous flow of constituent monomer, the growth inevitably saturates at a
423 plateau¹⁶. For both models, we therefore introduce a switch time t_1 after which the growth slowly
424 saturates sigmoidally over a time interval 5τ

425

$$426 \quad \frac{dA_{\text{lin}}(t)}{dt} = \begin{cases} r_1, & t_0 > t \\ r_2, & t_0 \leq t < t_1 \\ r_2 \frac{1}{1 + e^{\frac{5(t-\tau-t_1)}{\tau}}}, & t_1 \leq t \end{cases},$$

427

$$428 \quad \frac{dA_{\text{par}}(t)}{dt} = \begin{cases} r_1, & t_0 > t \\ \frac{1}{2}r_2 t, & t_0 \leq t < t_1 \\ \frac{1}{2}r_2 \frac{t}{1 + e^{\frac{5(t-\tau-t_1)}{\tau}}}, & t_1 \leq t \end{cases}.$$

429

430 Where we introduced the names A_{lin} and A_{par} referring to the linear-like and parabolic-like shape
431 of the two resulting growth curves. We found the anisotropic spherulites to fit best with A_{lin} and
432 the isotropic spherulites fit best with A_{par} .

433 When fitting an experimentally observed aggregate growth curve $\{A_i, t_i\}$, $i \in (0, N - 1)$ the
434 equations were numerically integrated from an initial timepoint (A_0, t_0) to the final timepoint
435 (A_{N-1}, t_{N-1}) . For each growth curve, the parameters $(r_1, r_2, t_0, t_1, \tau)$ were estimated with a chi2
436 fit. Each fit was run twice, the first fit was unweighted and were used to estimate the error bars
437 using the standard deviation of the residuals. The second fit used the residuals in a weighted chi2
438 fit to obtain the final fit parameters for the growth curve.

439

440 **Data availability**

441 All data sets used for figures are provided as source data in the manuscript. Source code and
442 executable can be found at <https://github.com/hatzakislabs/REPLOM-analysis-tool>. All source
443 data are available at <https://sid.erd.dk/sharelink/fje3exOlq2>.
444

445 **Author information**

446 **Corresponding Author**

447 * Vito Foderà, Email: vito.fodera@sund.ku.dk

448 * Nikos S. Hatzakis, Email: hatzakis@chem.ku.dk (NSH).

449 **Author Contributions**

450 M.Z, N.S.H and V.F wrote the paper with feedback from all authors. M.Z designed, carried out
451 and analysed all microscopy experiments, and prepared all samples. H.D.P wrote the automated
452 cluster finding and rates analysis algorithm. M.Z and X.Z did the ThT-fluorescence and turbidity
453 measurements. S.S-R.B calculated the resolution of REPLOM and fluorophore's lifetime. L.B and
454 A.Z helped with the mechanism explanation. N.S.H conceived the project idea, in collaboration
455 with V.F., and had the overall project management and strategy.

456 **Notes**

457 The authors declare no competing financial interest.

458 **Acknowledgment**

459 This work was funded by the Lundbeck foundation (grant R250-2017-1293 and R346-2020-1759)
460 for M.Z. Villum foundation young investigator fellowship (grant 10099), and the Carlsberg
461 foundation Distinguished Associate professor program (CF16-0797) and the NovoNordisk Center
462 for Biopharmaceuticals and Biobarriers in Drug Delivery (NNF16OC0021948) for N.S.H. Villum
463 foundation young investigator fellowship (grant 19175), the Novo Nordisk foundation
464 (NNF16OC0021948) and Lundbeck foundation (R155-2013-14113) for V.F. China Scholarship
465 Council (201709110108) for X.Z. Work at The Novo Nordisk Foundation Center for Protein
466 Research (CPR) that NSH is associated with, is funded by a generous donation from the Novo

467 Nordisk Foundation (Grant number NNF14CC0001). We thank Dr Y. Hu from Technical
468 University of Denmark for the help with SEM imaging.

469 N.S.H. and V.F are members of the Integrative Structural Biology Cluster (ISBUC) at the
470 University of Copenhagen.

471 REFERENCES

- 472 1 Chiti, F. & Dobson, C. M. Protein Misfolding, Functional Amyloid, and Human Disease.
473 *Annual Review of Biochemistry* **75**, 333-366,
474 doi:10.1146/annurev.biochem.75.101304.123901 (2006).
- 475 2 House, E., Jones, K. & Exley, C. Spherulites in Human Brain Tissue are Composed of
476 Beta Sheets of Amyloid and Resemble Senile Plaques. *Journal of Alzheimers Disease* **25**,
477 43-46, doi:10.3233/jad-2011-110071 (2011).
- 478 3 Exley, C. *et al.* Spherulites of Amyloid-beta(42) In Vitro and in Alzheimer's Disease.
479 *Journal of Alzheimers Disease* **20**, 1159-1165, doi:10.3233/jad-2010-091630 (2010).
- 480 4 Yumlu, S., Barany, R., Eriksson, M. & Röcken, C. Localized insulin-derived amyloidosis
481 in patients with diabetes mellitus: a case report. *Human Pathology* **40**, 1655-1660,
482 doi:<https://doi.org/10.1016/j.humpath.2009.02.019> (2009).
- 483 5 Jiang, Y. *et al.* Protein Spherulites for Sustained Release of Interferon: Preparation,
484 Characterization and in vivo Evaluation. *Journal of Pharmaceutical Sciences* **100**, 1913-
485 1922, doi:<https://doi.org/10.1002/jps.22403> (2011).
- 486 6 Vetri, V. & Foderà, V. The route to protein aggregate superstructures: Particulates and
487 amyloid-like spherulites. *FEBS Letters* **589**, 2448-2463,
488 doi:<http://doi.org/10.1016/j.febslet.2015.07.006> (2015).
- 489 7 Krebs, M. R. H. *et al.* The formation of spherulites by amyloid fibrils of bovine insulin.
490 *Proceedings of the National Academy of Sciences of the United States of America* **101**,
491 14420-14424, doi:10.1073/pnas.0405933101 (2004).
- 492 8 Lu, Z. P., Goh, T. T., Li, Y. & Ng, S. C. Glass formation in La-based La–Al–Ni–Cu–(Co)
493 alloys by Bridgman solidification and their glass forming ability. *Acta Materialia* **47**,
494 2215-2224, doi:[https://doi.org/10.1016/S1359-6454\(99\)00058-0](https://doi.org/10.1016/S1359-6454(99)00058-0) (1999).
- 495 9 Heaney, P. J. & Davis, A. M. Observation and Origin of Self-Organized Textures in
496 Agates. *Science* **269**, 1562-1565, doi:10.1126/science.269.5230.1562 (1995).
- 497 10 Hosier, I. L., Bassett, D. C. & Vaughan, A. S. Spherulitic Growth and Cellulation in
498 Dilute Blends of Monodisperse Long n-Alkanes. *Macromolecules* **33**, 8781-8790,
499 doi:10.1021/ma000946t (2000).
- 500 11 Kajioka, H., Hikosaka, M., Taguchi, K. & Toda, A. Branching and re-orientation of
501 lamellar crystals in non-banded poly(butene-1) spherulites. *Polymer* **49**, 1685-1692,
502 doi:<https://doi.org/10.1016/j.polymer.2008.01.066> (2008).
- 503 12 Garcia, G. A., Cohen, S. I. A., Dobson, C. M. & Knowles, T. P. J. Nucleation-
504 conversion-polymerization reactions of biological macromolecules with prenucleation
505 clusters. *Physical Review E* **89**, 032712, doi:10.1103/PhysRevE.89.032712 (2014).
- 506 13 Krebs, M. R. H., Bromley, E. H. C., Rogers, S. S. & Donald, A. M. The mechanism of
507 amyloid spherulite formation by bovine insulin. *Biophys. J.* **88**, 2013-2021,
508 doi:10.1529/biophysj.104.051896 (2005).

- 509 14 Domike, K. R. & Donald, A. M. Thermal Dependence of Thermally Induced Protein
510 Spherulite Formation and Growth: Kinetics of β -lactoglobulin and Insulin.
511 *Biomacromolecules* **8**, 3930-3937, doi:10.1021/bm7009224 (2007).
- 512 15 Ban, T. *et al.* Real-time and Single Fibril Observation of the Formation of Amyloid β
513 Spherulitic Structures. *Journal of Biological Chemistry* **281**, 33677-33683,
514 doi:10.1074/jbc.M606072200 (2006).
- 515 16 Domike, K. R. & Donald, A. M. Kinetics of spherulite formation and growth: Salt and
516 protein concentration dependence on proteins β -lactoglobulin and insulin. *International*
517 *Journal of Biological Macromolecules* **44**, 301-310,
518 doi:<https://doi.org/10.1016/j.ijbiomac.2008.12.014> (2009).
- 519 17 Foderà, V. & Donald, A. M. Tracking the heterogeneous distribution of amyloid
520 spherulites and their population balance with free fibrils. *The European Physical Journal*
521 *E* **33**, 273-282, doi:10.1140/epje/i2010-10665-4 (2010).
- 522 18 Toprakcioglu, Z., Challa, P., Xu, C. & Knowles, T. P. J. Label-Free Analysis of Protein
523 Aggregation and Phase Behavior. *ACS Nano* **13**, 13940-13948,
524 doi:10.1021/acsnano.9b05552 (2019).
- 525 19 Yagi, H., Ban, T., Morigaki, K., Naiki, H. & Goto, Y. Visualization and Classification of
526 Amyloid β Supramolecular Assemblies. *Biochemistry* **46**, 15009-15017,
527 doi:10.1021/bi701842n (2007).
- 528 20 Zimmermann, M. R. *et al.* Mechanism of Secondary Nucleation at the Single Fibril Level
529 from Direct Observations of A β 42 Aggregation. *Journal of the American Chemical*
530 *Society* **143**, 16621-16629, doi:10.1021/jacs.1c07228 (2021).
- 531 21 Andersen, C. B. *et al.* Branching in Amyloid Fibril Growth. *Biophysical Journal* **96**,
532 1529-1536, doi:<http://doi.org/10.1016/j.bpj.2008.11.024> (2009).
- 533 22 Vetri, V. *et al.* Ethanol Controls the Self-Assembly and Mesoscopic Properties of Human
534 Insulin Amyloid Spherulites. *The Journal of Physical Chemistry B* **122**, 3101-3112,
535 doi:10.1021/acs.jpcc.8b01779 (2018).
- 536 23 Johansson, P. K. & Koelsch, P. Label-free imaging of amyloids using their intrinsic linear
537 and nonlinear optical properties. *Biomed. Opt. Express* **8**, 743-756,
538 doi:10.1364/BOE.8.000743 (2017).
- 539 24 Pinotsi, D. *et al.* Direct Observation of Heterogeneous Amyloid Fibril Growth Kinetics
540 via Two-Color Super-Resolution Microscopy. *Nano Letters* **14**, 339-345,
541 doi:10.1021/nl4041093 (2014).
- 542 25 Cox, H., Georgiades, P., Xu, H., Waigh, T. A. & Lu, J. R. Self-Assembly of Mesoscopic
543 Peptide Surfactant Fibrils Investigated by STORM Super-Resolution Fluorescence
544 Microscopy. *Biomacromolecules* **18**, 3481-3491, doi:10.1021/acs.biomac.7b00465
545 (2017).
- 546 26 Kaminski Schierle, G. S. *et al.* In Situ Measurements of the Formation and Morphology
547 of Intracellular β -Amyloid Fibrils by Super-Resolution Fluorescence Imaging. *Journal of*
548 *the American Chemical Society* **133**, 12902-12905, doi:10.1021/ja201651w (2011).
- 549 27 Pinholt, H. D., Bohr, S. S.-R., Iversen, J. F., Boomsma, W. & Hatzakis, N. S. Single-
550 particle diffusional fingerprinting: A machine-learning framework for quantitative
551 analysis of heterogeneous diffusion. *Proceedings of the National Academy of Sciences*
552 **118**, e2104624118, doi:10.1073/pnas.2104624118 (2021).
- 553 28 Thomsen, J. *et al.* DeepFRET, a software for rapid and automated single-molecule FRET
554 data classification using deep learning. *eLife* **9**, doi:10.7554/eLife.60404 (2020).

- 555 29 Stella, S. *et al.* Conformational Activation Promotes CRISPR-Cas12a Catalysis and
556 Resetting of the Endonuclease Activity. *Cell* **175**, 1856-1871.e1821,
557 doi:<https://doi.org/10.1016/j.cell.2018.10.045> (2018).
- 558 30 Jensen, S. B. *et al.* Biased cytochrome P450-mediated metabolism via small-molecule
559 ligands binding P450 oxidoreductase. *Nat. Commun.* **12**, 2260, doi:10.1038/s41467-021-
560 22562-w (2021).
- 561 31 Malle, M. G. *et al.* Single particle combinatorial multiplexed liposome fusion mediated
562 by DNA. *bioRxiv*, 2021.2001.2019.427313, doi:10.1101/2021.01.19.427313 (2021).
- 563 32 Huang, B., Wang, W., Bates, M. & Zhuang, X. Three-Dimensional Super-Resolution
564 Imaging by Stochastic Optical Reconstruction Microscopy. *Science* **319**, 810-813,
565 doi:10.1126/science.1153529 (2008).
- 566 33 Hayashi, S. & Okada, Y. Ultrafast superresolution fluorescence imaging with spinning
567 disk confocal microscope optics. *Molecular Biology of the Cell* **26**, 1743-1751,
568 doi:10.1091/mbc.E14-08-1287 (2015).
- 569 34 Foderà, V., van de Weert, M. & Vestergaard, B. Large-scale polymorphism and auto-
570 catalytic effect in insulin fibrillogenesis. *Soft Matter* **6**, 4413-4419,
571 doi:10.1039/C0SM00169D (2010).
- 572 35 Foderà, V. *et al.* Self-Organization Pathways and Spatial Heterogeneity in Insulin
573 Amyloid Fibril Formation. *The Journal of Physical Chemistry B* **113**, 10830-10837,
574 doi:10.1021/jp810972y (2009).
- 575 36 Foderà, V., Zaccone, A., Lattuada, M. & Donald, A. M. Electrostatics Controls the
576 Formation of Amyloid Superstructures in Protein Aggregation. *Physical Review Letters*
577 **111**, 108105, doi:10.1103/PhysRevLett.111.108105 (2013).
- 578 37 Rogers, S. S., Krebs, M. R. H., Bromley, E. H. C., van der Linden, E. & Donald, A. M.
579 Optical Microscopy of Growing Insulin Amyloid Spherulites on Surfaces In Vitro.
580 *Biophysical Journal* **90**, 1043-1054, doi:10.1529/biophysj.105.072660 (2006).
- 581 38 Shtukenberg, A. G., Punin, Y. O., Gunn, E. & Kahr, B. Spherulites. *Chemical Reviews*
582 **112**, 1805-1838, doi:10.1021/cr200297f (2012).
- 583 39 Gránásy, L., Pusztai, T., Tegze, G., Warren, J. A. & Douglas, J. F. Growth and form of
584 spherulites. *Physical Review E* **72**, 011605, doi:10.1103/PhysRevE.72.011605 (2005).
- 585 40 Shen, Y. *et al.* Biomolecular condensates undergo a generic shear-mediated liquid-to-
586 solid transition. *Nature Nanotechnology* **15**, 841-847, doi:10.1038/s41565-020-0731-4
587 (2020).
- 588 41 Song, S. *et al.* Spherulite-like Micelles. *Angewandte Chemie International Edition n/a*,
589 doi:<https://doi.org/10.1002/anie.202101177>.
- 590 42 Galkin, O. & Vekilov, P. G. Mechanisms of Homogeneous Nucleation of Polymers of
591 Sick Cell Anemia Hemoglobin in Deoxy State. *Journal of Molecular Biology* **336**, 43-
592 59, doi:<https://doi.org/10.1016/j.jmb.2003.12.019> (2004).
- 593 43 Elsharkawy, S. *et al.* Protein disorder-order interplay to guide the growth of hierarchical
594 mineralized structures. *Nature Communications* **9**, doi:ARTN 214510.1038/s41467-018-
595 04319-0 (2018).
- 596 44 Moses, M. E. *et al.* Single-Molecule Study of *Thermomyces lanuginosus* Lipase in a
597 Detergency Application System Reveals Diffusion Pattern Remodeling by Surfactants
598 and Calcium. *ACS Appl. Mater. Interfaces* **13**, 33704-33712,
599 doi:10.1021/acsami.1c08809 (2021).

600 45 Bohr, S. S. R. *et al.* Direct observation of *Thermomyces lanuginosus* lipase diffusional
601 states by Single Particle Tracking and their remodeling by mutations and inhibition. *Sci*
602 *Rep-Uk* **9**, 16169, doi:10.1038/s41598-019-52539-1 (2019).

603 46 Betzig, E. *et al.* Imaging Intracellular Fluorescent Proteins at Nanometer Resolution.
604 *Science* **313**, 1642-1645, doi:10.1126/science.1127344 (2006).

605 47 Gordon, M. P., Ha, T. & Selvin, P. R. Single-molecule high-resolution imaging with
606 photobleaching. *Proceedings of the National Academy of Sciences of the United States of*
607 *America* **101**, 6462-6465, doi:10.1073/pnas.0401638101 (2004).

608 48 Qu, X., Wu, D., Mets, L. & Scherer, N. F. Nanometer-localized multiple single-molecule
609 fluorescence microscopy. *Proceedings of the National Academy of Sciences of the United*
610 *States of America* **101**, 11298-11303, doi:10.1073/pnas.0402155101 (2004).

611 49 Burnette, D. T., Sengupta, P., Dai, Y., Lippincott-Schwartz, J. & Kachar, B.
612 Bleaching/blinking assisted localization microscopy for superresolution imaging using
613 standard fluorescent molecules. *Proceedings of the National Academy of Sciences* **108**,
614 21081-21086, doi:10.1073/pnas.1117430109 (2011).

615 50 Ries, J. *et al.* Superresolution Imaging of Amyloid Fibrils with Binding-Activated
616 Probes. *ACS Chemical Neuroscience* **4**, 1057-1061, doi:10.1021/cn400091m (2013).

617 51 Cowan, N. B. & Ivezić, Ž. The Environment of Galaxies at Low Redshift. *The*
618 *Astrophysical Journal* **674**, L13-L16, doi:10.1086/528986 (2008).

619 52 Goldenfeld, N. Theory of spherulitic crystallization. *Journal of Crystal Growth* **84**, 601-
620 608, doi:[https://doi.org/10.1016/0022-0248\(87\)90051-0](https://doi.org/10.1016/0022-0248(87)90051-0) (1987).

621 53 Majumder, S., Busch, H., Poudel, P., Mecking, S. & Reiter, G. Growth Kinetics of Stacks
622 of Lamellar Polymer Crystals. *Macromolecules* **51**, 8738-8745,
623 doi:10.1021/acs.macromol.8b01765 (2018).

624 54 Tanaka, H. & Nishi, T. New Types of Phase Separation Behavior during the
625 Crystallization Process in Polymer Blends with Phase Diagram. *Physical Review Letters*
626 **55**, 1102-1105, doi:10.1103/PhysRevLett.55.1102 (1985).

627 55 Buell, A. K. *et al.* Detailed Analysis of the Energy Barriers for Amyloid Fibril Growth.
628 *Angewandte Chemie International Edition* **51**, 5247-5251,
629 doi:<https://doi.org/10.1002/anie.201108040> (2012).

630 56 Cohen, S. I. A. *et al.* Distinct thermodynamic signatures of oligomer generation in the
631 aggregation of the amyloid- β peptide. *Nat Chem* **10**, 523-531, doi:10.1038/s41557-018-
632 0023-x (2018).

633 57 Sang, J. C. *et al.* Super-resolution imaging reveals α -synuclein seeded aggregation in SH-
634 SY5Y cells. *Communications Biology* **4**, 613, doi:10.1038/s42003-021-02126-w (2021).

635 58 Chen, W. *et al.* Fluorescence Self-Quenching from Reporter Dyes Informs on the
636 Structural Properties of Amyloid Clusters Formed in Vitro and in Cells. *Nano Letters* **17**,
637 143-149, doi:10.1021/acs.nanolett.6b03686 (2017).

638 59 Huang, B., Jones, S. A., Brandenburg, B. & Zhuang, X. Whole-cell 3D STORM reveals
639 interactions between cellular structures with nanometer-scale resolution. *Nature Methods*
640 **5**, 1047, doi:10.1038/nmeth.1274
641 <https://www.nature.com/articles/nmeth.1274#supplementary-information> (2008).

642 60 Ovesný, M., Křížek, P., Borkovec, J., Švindrych, Z. & Hagen, G. M. ThunderSTORM: a
643 comprehensive ImageJ plug-in for PALM and STORM data analysis and super-resolution
644 imaging. *Bioinformatics* **30**, 2389-2390, doi:10.1093/bioinformatics/btu202 (2014).

- 645 61 Beheiry, M. E. & Dahan, M. ViSP: representing single-particle localizations in three
646 dimensions. *Nature Methods* **10**, 689, doi:10.1038/nmeth.2566
647 <https://www.nature.com/articles/nmeth.2566#supplementary-information> (2013).
- 648 62 Ogi, H. *et al.* Ultrafast propagation of β -amyloid fibrils in oligomeric cloud. *Sci Rep-Uk*
649 **4**, 6960, doi:10.1038/srep06960 (2014).
- 650 63 Thomsen, R. P. *et al.* A large size-selective DNA nanopore with sensing applications.
651 *Nat. Commun.* **10**, 5655, doi:10.1038/s41467-019-13284-1 (2019).
- 652

Supplementary Files

This is a list of supplementary files associated with this preprint. Click to download.

- [REPLOMSI.pdf](#)
- [SupplementaryMovie1.mp4](#)
- [SupplementaryMovie2.mp4](#)
- [SupplementaryMovie3.mp4](#)
- [SupplementaryMovie4.mp4](#)
- [SupplementaryMovie5.mp4](#)
- [SupplementaryMovie6.mp4](#)
- [SupplementaryMovie7.mp4](#)
- [SupplementaryMovie8.mp4](#)